is linked to the fact that the near field of the antenna concentrates in the sandwich, and couples less to the arm. This was confirmed by calculating the electric field (*E*-field) distributions around the body model at the FCC midband 6.85 GHz. Figure 3 illustrates the normalized *E*-field distribution in a logarithmic scale in the *x*-*z* and *y*-*z* planes. It shows less field strength toward the body, even when these small loads are applied. The colors representing the normalized *E*-field go from blue (weak *E*-field) to green to yellow to red (strong *E*-field). Simulations show that loading also slightly improves the antenna efficiency in proximity to the body. It is worth mentioning that due to the high permittivity of the human tissues, which acts as a sort of additional substrate, a downshift in the lower edge of the −10 dB frequency bandwidth is observed when comparing results in free space and in presence of the body. In general, if the distance between the antenna and the body is reduced, the bandwidth shift increases. Nevertheless, the overall agreement between the results is acceptable. Based on the measurement results, loading the antenna increases the antenna impedance matching by ∼22% with respect to the unloaded antenna, and clearly shows the improvement caused by applying this technique.

Then, the distance was increased to 7 mm with the use of an extra 4-mm spacer. This was intended to check the changes in the antenna behavior as it moves away from the body. Measurement results are illustrated in Figure 2. It can be seen that when the distance increases from 3 to 7 mm results become more similar to those obtained in free space. Therefore, as expected, the antenna impedance matching increases: 4.5% for the loaded and 28% for the unloaded prototype. As mentioned, the loading does not detune the antenna in free space; it is thus expected that the total bandwidth for the loaded and unloaded antennas approaches the same value when moving away from the body. This fact was confirmed, as seen in Figure 2, the total bandwidth for the loaded and unloaded prototypes are 6.7 and 6.9 GHz, respectively. Thus, applying the technique could result in a significant improvement near the body, and the loading effect decreases when the antenna moves away from the body, as expected.

4. CONCLUSION

This article presents a technique to enhance the impedance matching of an antenna when it is placed close to the human body making use of dielectric sandwich loading. This lessens the body influence due to the reactive fields' confinement in the dielectric loads without inducing side effects on the antenna performance, that is, efficiency decrease. A loaded UWB antenna prototype was compared to an unloaded one through measurements both in free space and near a human arm. Free space results confirm that loading neither detune the antenna nor decrease the efficiency. It was found that in a body proximity scenario for 3-mm distance between the antenna and the arm surface, loading the antenna increases the impedance matching by 22%. These results clearly show that this technique leads to suitable solutions for designing antennas for future WBAN applications.

ACKNOWLEDGMENTS

This work was supported by the Portuguese Fundação para a Ciência e a Tecnologia (FCT) project PEST–OE/EEI/LA0008/2011. The work of Nuno Pires is supported by the FCT grant SFRH/BD/51066/2010 and Mohsen Koohestani by the FCT grant SFRH/BD/51445/2011.

REFERENCES

1. N. Chahat, M. Zhadobov, R. Sauleau, and K. Ito, A compact UWB antenna for on–body applications, IEEE Trans Antennas Propag 59 (2011).
2. P.S. Hall and Y. Hao, Antennas and propagation for Body-Centric Wireless communications, Artech House, Norwood, MA, 2006.
3. R. Augustine, Electromagnetic modelling of human tissues and its application on the interaction between antenna and human body in the BAN context, PhD thesis, Université Paris-Est Marne-la-Vallée, 2009.
4. M. Koohestani, N. Pires, A.K. Skrivervik, and A.A. Moreira, Influence of the human body on a new coplanar-fed ultra-wideband antenna, In: The 6th EuCAP, Prague, Czech Republic, 2012.
5. T.S.P. See and N.C. Zhi, Experimental characterization of UWB antennas for on-body communications, IEEE Trans Antennas Propag 57 (2009).
6. B.A. Kramer, C. Chen, and J.L. Volakis, Design and performance of an ultra-wideband ceramic-loaded slot spiral, In: IEEE Antennas and Propagation Society International Symposium, Monterey, CA, 2004.
7. Y.-P. Zhang, T.K.-C. Lo, and Y.-M. Hwang, A dielectric-loaded miniature antenna for microcellular and personal communications, In: IEEE Antennas and Propagation Society International Symposium, Newport Beach, CA, 1995.
8. A.A. Moreira, N. Pires, N. Serro, and R. Santos, Ultra wideband dielectric sandwich loaded antennas, In: The 3rd EuCAP, Berlin, Germany, 2009.
9. N. Pires, M. Letizia, S. Boyes, Y. Lu, Y. Huang, A.K. Skrivervik, and A.A. Moreira, Improved design of an Ultra-wideband universal serial bus device mounted antenna based on comparative radiation efficiency measurements, In: The 5th EuCAP, Rome, Italy, 2011.
10. M. Koohestani, N. Pires, A.K. Skrivervik, and A.A. Moreira, Influence of dielectric loading on the fidelity factor of an ultra wideband monopole antenna, In: LAPC, Loughborough, United Kingdom, 2012.
11. M. Koohestani, N. Pires, A.K. Skrivervik, and A.A. Moreira, Performance study of an UWB antenna in proximity to a human arm, IEEE Antennas Wireless Propag Lett, in press.
12. N. Pires, C. Mendes, M. Koohestani, A.K. Skrivervik, and A.A. Moreira, Radiation efficiency of a coplanar-fed ultra-wideband antenna, In: IEEE AP-S/USNC-URSI Symposium, Chicago, IL, 2012.

COMPRESSED SENSING-BASED IMAGING OF MILLIMETER-WAVE ISAR DATA

Sevket Demirci and Caner Ozdemir
Department of Electrical-Electronics Engineering, Mersin University, 33343, Yenisehir, Mersin, Turkey; Corresponding author: sdemirci@mersin.edu.tr

Received 19 April 2013

ABSTRACT: *High-resolution radar imaging requires wide bandwidths and highly dense samplings of both time/frequency and spatial domains. However, the rapidly developing field of compressive sensing (CS) breaks this rule and paves a way for simultaneously achieving high-resolution imaging with a significantly reduced number of samples. Although CS is seemed to be an intuitively attractive approach, the ongoing studies have shown the application of CS to synthetic aperture radar (SAR) data to be a challenging task in practice. In this work, as a contribution to these efforts, we address the potential use of CS in millimeter-wave inverse SAR (ISAR) imaging. Various simulation and experimental imaging results are presented to demonstrate the validity and the robustness of the proposed CS-based reconstruction from very limited samples.* © 2013 Wiley Periodicals, Inc. Microwave Opt Technol Lett 55:2967–2972, 2013; View this article online at wileyonlinelibrary.com. DOI 10.1002/mop.27969

Key words: *compressed sensing; compressive sampling; synthetic aperture radar; inverse synthetic aperture radar*

1. INTRODUCTION

Ground-based synthetic aperture radar (SAR) imaging has popular applications such as concealed weapon detection (CWD) [1,2], through-the-wall radar imaging (TWRI) [3,4], foreign object debris [5] detection, and so forth. These applications, however, generally face some difficulties that mainly arise from the demands for high-resolution and nearly real-time imaging. Specifically, high-resolution imaging requires large bandwidths in data collection and hence high-sampling rates along both time/frequency and spatial directions. Therefore, a vast amount of data has to be acquired and processed, especially when dealing with three-dimensional (3D) imaging systems, which may further limit the feasibility of fast imaging and reducing data storage burden. The conventional approach to this problem assumes sampling and compression as two separate processes and applies compression to the full-sampled signal [6]. On the other hand, compressed sensing (CS) introduced in [7,8] has a new compression/decompression approach which directly acquires the compressed representation of the signal. According to CS theory, it is possible to reconstruct sparse or compressible signals from a small set of linear measurements. Besides, if properly selected (i.e., random, noisy-like), the number of these measurements can be much smaller than the Nyquist rate which obviously provide distinct advantages in terms of data acquisition and processing.

Consequently, the possible use of CS in SAR imaging has recently attracted a growing interest [9–27]. In [9–15], the CS concept has been tested for traditional airborne/spaceborne SAR imaging and through the simulation [9–12] and the experimental [13–15] results. Circular SAR (CSAR) imaging is another modality that has also received considerable attention for its CS applicability [16–20] mainly due to its substantial data outcome. Various numerical [16–18] and real [19,20] examples have been presented for this challenging task of CSAR imaging. Some ground-based imaging results for TWRI [21–25], linear-SAR [26], and inverse SAR (ISAR) [27] applications have also been demonstrated. On the whole, these studies have shown the application of CS to SAR imaging to be challenging in practice and highly depends on the sparsity of the encountered SAR signal. This sparsity; in turn, is highly related to the investigated scene and employed imaging geometry. For example, the backscattering signal is expected to have high sparsity due to the existence of a small number of strong scattering centers for turntable-based ISAR or equivalently ground-based annular/circular motion SAR imaging [28]. Thus, the CS approach may be readily exploited in numerous applications that utilize these scanning geometries, such as in CWD problem.

In this article, the utility of using CS in millimeter-wave ISAR imaging is studied. The simulation and experimental results are demonstrated to assess the potential uses, benefits, and limitations of CS in the case of a highly undersampled, W-band ISAR data. The article is organized as follows: next section contains a brief overview of the CS theory. In the third section, the echo model for a 2D ISAR signal is derived. In the next section, the CS-based reconstruction technique is described based on this constructed model. Fifth section presents the simulation and experimental results for the millimeter-wave scattering responses of various threat-like targets. The conclusions and discussions are given in the final section.

2. COMPRESSED SENSING BASICS

The CS theory basically states that a discrete signal of interest expressed as a vector $\sigma \in \mathbb{C}^Q$ can be exactly reconstructed with

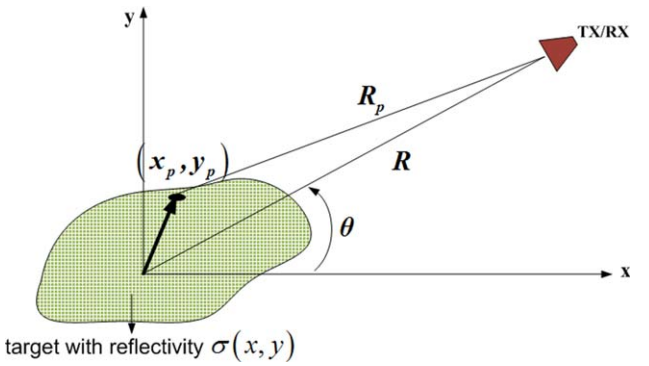

Figure 1 Geometry for a 2D monostatic ISAR imaging. [Color figure can be viewed in the online issue, which is available at wileyonlinelibrary.com]

a few number of samples compared to the Nyquist rate, provided that it is compressible (i.e., sparse) in some orthonormal basis. Hence, σ can be represented as $\sigma = \mathbf{\Psi}\alpha$ where $\mathbf{\Psi} \in \mathbb{C}^{Q \times Q}$ is a matrix whose columns hold the basis vectors and $\alpha \in \mathbb{C}^Q$ is the coefficient sequence of σ which have only $S \ll Q$ nonzero components. Within CS terminology, the signal is assumed to be collected through linear projections, $y = \Phi\sigma$, where $y \in \mathbb{C}^J$ is a vector of measurement samples and $\Phi \in \mathbb{C}^{J \times Q}$ is known as the measurement matrix with $J < Q$. Noting the compressed representation of σ, this linear measurement model can also be described as

$$y = \Phi\sigma = \mathbf{\Phi\Psi}\alpha = \Theta\alpha \tag{1}$$

where $\Theta = \mathbf{\Phi\Psi}$ is a $J \times Q$ matrix. The CS theory tells us that if Θ satisfies the restricted isometry property (RIP), which is also closely related to the mutual incoherence between the measurement matrix Φ and the representation basis $\mathbf{\Psi}$, a sparse approximation of the unknown vector α can be obtained through Eq. (1) [7,8]. This recovery can be implemented by searching for the sparsest vector $\tilde{\alpha}$ for the given measurements y and is generally referred to as the optimization problem with the ℓ_0-norm, which is expressed as "$\alpha = \arg\min \tilde{\alpha} \|\tilde{\alpha}\|$ subject to $y = \mathbf{\Phi\Psi}\alpha$" where the ℓ_0-norm denoted by $\|\cdot\|_0$ represents the number of nonzero elements in a vector. Solving this; however, is a NP-hard (nondeterministic polynomial-time hard) problem which cannot be easily achieved in practice. Nevertheless, the sparse solution can be alternatively found by either replacing ℓ_0-norm minimization with an easier ℓ_1-norm minimization or by using a greedy algorithm such as orthogonal matching pursuit. Finally, it is worth noting that for random, noise-like measurement matrices Φ and for a total of j measurements satisfying $J \geq O(S \log(Q/S))$, a unique stable solution for the S-sparse signal α can be obtained with high probability [8].

3. ISAR SIGNAL MODEL

Data collection geometry for a 2D monostatic ISAR imaging is shown in Figure 1. The target is represented by a reflectivity function $\sigma(x, y)$ and illuminated by an antenna positioned at the Cartesian coordinates $(x, y) = (R\cos\theta,\ R\sin\theta)$ where R is the range from the antenna location to the scene center (i.e., coordinate origin) and θ is the instantaneous look-angle. Assuming the target is composed of a total of P number of independent point scatterers, the received echo signal at some look-angle θ can be expressed, for a frequency domain radar system as

$$y_\theta(k)=\sum_{p=1}^{P}\sigma_p\exp\{-jkR_p(\theta)\} \tag{2}$$

where k is the wavenumber defined for the two-way propagation as $k=4\pi f/c$, f is the frequency, c is the speed of light, and $R_p(\theta)$ is the range from the antenna location to the p-th scatterer. Considering a near-field scanning geometry, $R_p(\theta)$ can be written as

$$R_p(\theta)=\sqrt{(x_p-x)^2+(y_p-y)^2} \tag{3}$$

where (x_p,y_p) denotes the coordinates of the p-th scatterer for a specific rotation or look-angle θ and (x,y) is the coordinates of the fixed antenna position. Hence, a 2D ISAR data $\boldsymbol{y}(\boldsymbol{k},\theta)$ is acquired by measuring the target response over various look-angles.

4. ISAR IMAGING VIA CS

Considering again the geometry shown in Figure 1, let us assume that the frequency (wavenumber) and the angular data are collected for a total of K and L points, respectively, which both obey the Shannon/Nyquist criteria. Thus, a $K\times L$ size matrix data of the ISAR echo signal $\boldsymbol{y}(\boldsymbol{k},\theta)$ is produced. By dividing the 2D image scene into $M\times N$ pixels, the received signal also given in Eq. (2) can be written for this case as

$$y(k_u,\theta_v)=\sum_{n=1}^{N}\sum_{m=1}^{M}\sigma\,(x_{mn},y_{mn})\cdot\exp\{-jk_uR_{mn}(\theta_v)\} \tag{4}$$

where x_{mn}, y_{mn} denotes the pixel coordinates, $R_{mn}(\theta_v)=\sqrt{(x_{mn,\theta_v}-x)^2+(y_{mn,\theta_v}-y)^2}$, $u=1,2,\ldots,K$ and $v=1,2,\ldots,L$. Let us define $\mathbf{A}\in\mathbb{C}^{KL\times MN}$ as the measurement matrix of the echo signal with elements $A_{uv}(x_{mn},y_{mn})=\exp\{-jk_uR_{mn}(\theta_v)\}$ and reshape 2D matrices $\mathbf{y}\in\mathbb{C}^{K\times L}$ and $\sigma\in\mathbb{C}^{M\times N}$ as 1D vectors that are formed by stacking their columns. Then, Eq. (4) can be written in vector form as

$$y=\boldsymbol{A}\sigma+n \tag{5}$$

where n represents the additive noise. It is assumed that the target reflectivity σ is a S-sparse vector, that is, it has only $S(S\ll MN)$ number of entries that contain most of the information of the scene. This reflectivity vector can be expressed in an orthonormal basis $\boldsymbol{\Psi}\in\mathbb{C}^{MN\times MN}$ as

$$\sigma=\boldsymbol{\Psi}\alpha \tag{6}$$

where α is the coefficient sequence of σ whose nonzero entries represent the S strongest scattering centers. So, the linear representation model of the measured signal given in Eq. (5) can be written as

$$y=\boldsymbol{A}\boldsymbol{\Psi}\alpha+n \tag{7}$$

Now, according to the CS theory, it is possible to completely reconstruct the sparse vector α with a very small number of samples of the measured signal y. Thus, J $(S\le J<<KL)$ rows of the measurement matrix A and corresponding values of y can be selected randomly to confine the RIP condition as well. In this case, new measured signal model for the CS reconstruction can be obtained as

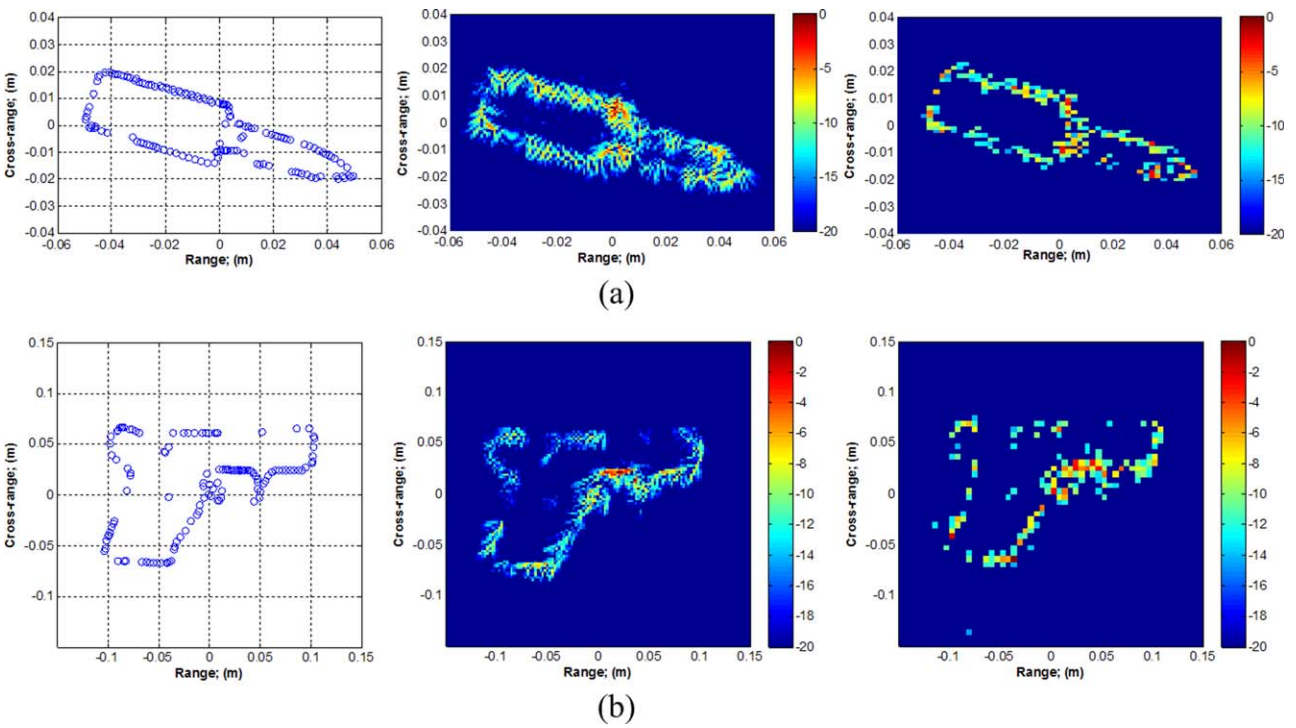

Figure 2 Images of the simulation targets (left: point scatterer model, middle: BP result, right: CS result). (a) a knife and (b) a handgun. [Color figure can be viewed in the online issue, which is available at wileyonlinelibrary.com]

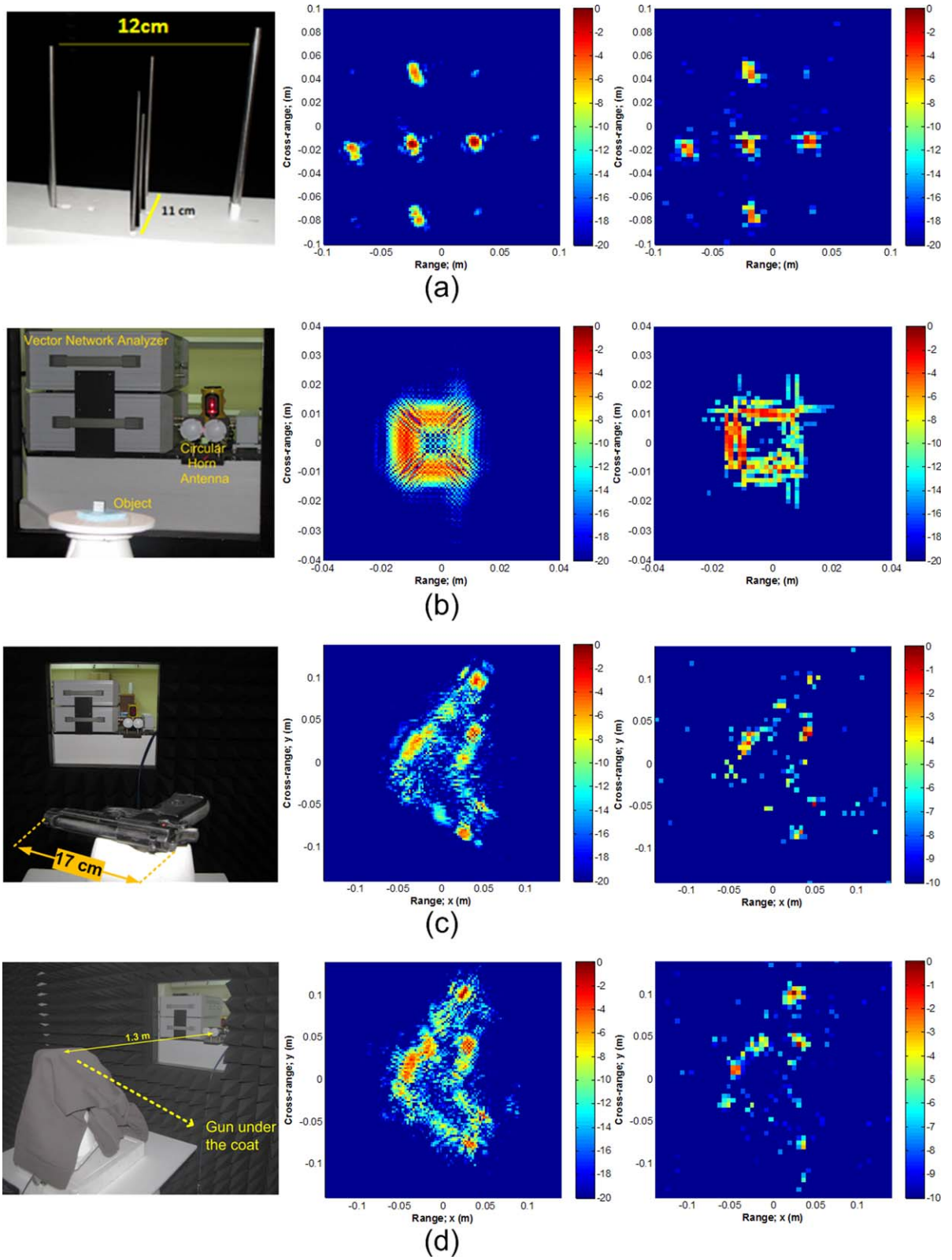

Figure 3 Photos and imaging results of various target scenes (left: sample photo of the target scene, middle: BP result, right: CS result). (a) Five metal cylinders, (b) 2 cm metal cube, (c) A metal handgun, and (d) a metal handgun covered with a warm winter coat. [Color figure can be viewed in the online issue, which is available at wileyonlinelibrary.com]

$$y_p = \Phi \boldsymbol{A} \boldsymbol{\Psi} \alpha + n = \Theta \alpha + n \tag{8}$$

where $\Phi \in \mathbb{R}^{J \times KL}$ is the orthonormal basis matrix formed by random selection of the J rows of a $KL \times KL$ size identity matrix and Θ is the final measurement matrix. With this constructed model for the ISAR echo signal, a sparse approximation of α can be found via one kind of optimization problem mentioned in section 2, from which the desired complex reflectivity function σ can be subsequently derived.

5. SIMULATION AND MEASUREMENT RESULTS

In this section, we demonstrate the performance and effectiveness of our CS-based reconstruction technique on both the synthetic and the real-ISAR data. The main attention was given to the assessment of the CS usage in a typical CWD problem. Therefore, near-field thread-like objects that were illuminated with W-band (75–110 GHz) radiation was considered throughout the study. Despite the 3D imaging requirements of these applications; first, we considered here only the 2D imaging geometry to validate and evaluate the CS approach to have a simpler configuration. In all examples, the sparse approximations of the target reflectivity functions were found by using a widely known greedy reconstruction algorithm, namely COSAMP [29]. Imaging results of a near-field back-projection (BP) algorithm [30] were obtained as well for comparison purposes. It is also worth noting that, all BP images were reconstructed onto 128×128 data-grid, whereas the CS ones were obtained for 55×55 data-grid due to the memory-size limitations.

Two simulation examples were studied under point scattering assumption of isotropic uniform reflectivity. In the first example, a knife-like object was taken as the target and represented with 139 perfect point scatterers of equal magnitudes as shown in Figure 2(a). Assuming near-field illumination, data were collected for the frequency span of $f=80$ *to* 100 GHz sampled at $K=401$ points and the angular span of $\theta=0$ *to* 180° sampled at $L=721$ points. Thus, $K\times L=289121$ measurements of (f,θ) pair were acquired. The results of the application of the traditional BP algorithm and the proposed CS-based algorithm are shown in the middle and right images of Figure 2(a), respectively. The CS result was obtained by using only the 2200 random samples of the total (f,θ) measurements which correspond to 0.76% of the whole data. Comparing with the BP result, the CS method yields an accurate representation of the scattering mechanisms with appropriate intensity levels. In the second example, a handgun was assumed and modeled by 123 perfect point scatterers whose coordinates are shown in Figure 2(b). In this case, the frequency bandwidth was reduced to 10 GHz ranging from 85 to 95 GHz, and the angular width was also reduced to 90°, spanning from 0° to 90°. Considering the spatial extents of the handgun, total number of the frequency and the angular sampling points were again set to $K=401$ and $L=721$ to satisfy the Shannon/Nyquist criteria. The middle image of Figure 2(b) shows the reference BP result; whereas, the right image shows the reconstructed image using CS with 5200 samples (i.e., 1.79% of the whole dataset). As before, the target was imaged accurately thereby demonstrating the success of the CS method on the synthetic data.

The real experiments were conducted within the indoor anechoic chamber facility of the International Laboratory for High Technologies (ILHT) at Scientific and Research Council of Turkey-Marmara Research Center (TUBITAK-MRC). As shown from the pictures given in Figure 3, the system involves a vector network analyzer with the stepped frequency continuous wave operation, two circular horn antennas set to be operated at quasimonostatic configuration, a turntable and a styrofoam block onto which targets are mounted. In all experiments, the antenna-to-target distance was kept to a fixed value of 1.3 m and the collected data were calibrated by the help of a metal sphere. Four different target scenes whose pictures are given in the left column of Figure 3 are considered. The corresponding imaging results for the BP and the CS method are shown in the middle and right columns, respectively. In the first experiment, the scene with five metal cylinders was tested. Due to the point-like reflection mechanism of these targets, the reflectivity function was expected to have high sparsity and to be easily reconstructed by the CS approach. The ISAR data were collected for the frequency range of $f=80$ to 102.06 GHz with $K=256$ sampling points and the angular coverage of $\theta=0$ *to* 60° with $L=241$ points. The CS result obtained by using 9.4% of the received data is given in the right image of Figure 3(a). Comparing with the BP result, it is shown that actual target positions and amplitudes are clearly reconstructed, while a few false mappings can also be seen within the dynamic range of -20 dB. In the second experiment, a 2 cm^3 metal cube was used as a slightly more complex scene. The scattered radiation was collected with the following parameters: $f=80$ *to* 100 GHz sampled at $K=256$ points and $\theta=0\sim360^\circ$ sampled at $L=361$ points. The CS result with 6.27% random echo samples indicates the efficient reconstruction of the target shape of very small size. In the third experiment, a metal handgun was used to evaluate the performance of the CS technique on ISAR imaging for a more complex test scene. A vast size of data with $256\times1441=368.896$ measurement points were acquired for the investigated bandwidth between 80 and 90 GHz and for the whole angular width from 0° to 360°. The middle image of Figure 3(c) shows the result of the BP processing of the all samples, whereas the right image shows the results of the CS processing of the randomly selected 1.57% samples of the whole collected dataset. It can be commented that although the CS-based imagery retains considerably less target information, it is still possible to identify the target shape from the accurate representation of the dominant scattering centers. In the last experiment, a handgun was covered with a warm winter coat and scanned by using the same parameters of the previous experiment. This arrangement leads to quite disturbing effects on the target response which is evident from the BP imaging results given in the relevant figures of Figures 3(c) and 3(d). Nevertheless, the CS approach is shown to be not affected by this degradation and provide sufficient features to effectively image the target for detection and identification despite the negative effects caused by the covering material of the handgun.

6. CONCLUSION

In this study, the feasibility of using CS for near-field millimeter-wave ISAR imaging has been investigated through the numerical and the measurement examples. Simulation results were obtained under the ideal isotropic point scattering assumption and yielded almost perfect imagery wherein the targets were successfully identified. The experimental results obtained within an anechoic chamber room mostly demonstrate the validity of the CS technique especially for less complex scenes composed of cylindrical and cube shaped targets. Nevertheless, as it can be shown from the imaging results of the handgun target, the increasing complexity of the test scene may somewhat limit the performance of the CS method. As a final note, although it is not presented here, it was also observed that increasing the number of random samples would have a beneficial impact on the success of the CS-based reconstruction. Yet, satisfactory results has also been achieved even for the case of very few number of samples (e.g., 1.57% of data).

ACKNOWLEDGMENTS

The authors are grateful to International Laboratory for High Technologies (ILHT) of TUBITAK Marmara Research Center for providing laboratory facilities for the conducted experiments.

The authors also wish to acknowledge Mr. Enes Yigit and the ILHT employees; Mr. Harun ÇETİNKAYA and Mr. Mustafa TEKBAŞ for their contributions to the experimental study.

REFERENCES

1. D.J. Daniels, Radar systems, In: EM detection of concealed targets, Chapter 5, John Wiley & Sons, Inc.: Hoboken, NJ, 2009.
2. I. Jaeger, L. Zhang, J. Stiens, H. Sahli, and R. Vounckx, Millimeter wave inspection of concealed objects, Microwave Opt Technol Lett 49 (2007), 2733–2737.
3. E. Engin, B. Ciftcioglu, M. Ozcan, and I. Tekin, High resolution ultrawideband wall penetrating radar, Microwave Opt Technol Lett 49 (2007), 320–325.
4. C.R.P. Dionisio, S. Tavares, M. Perotoni, and S. Kofuji, Experiments on through-wall imaging using ultra wideband radar, Microwave Opt Technol Lett 54 (2012), 339–344.
5. E. Yigit, S. Demirci, A. Unal, C. Ozdemir, and A. Vertiy, Millimeter-wave ground-based synthetic aperture radar imaging for foreign object debris detection: Experimental studies at short ranges, J Infrared Millim Terahertz Waves 33 (2012), 1227–1238.
6. U. Benz, K. Strodl, and A. Moreira, A comparison of several algorithms for SAR raw data compression, IEEE Trans Geosci Remote Sens 33 (1995), 1266–1276.
7. E. Candes, J. Romberg, and T. Tao, Stable signal recovery from incomplete and inaccurate measurements, Commun Pure Appl Math 59 (2006), 1207–1223.
8. D.L. Donoho, Compressed sensing, IEEE Trans Inform Theory 52 (2006), 1289–1306.
9. R. Baraniuk and P. Steeghs, Compressive radar imaging, In: 2007 IEEE Radar Conference, Waltham, Massachusetts, April 17–20, 2007, pp. 128–133.
10. M.A. Herman and T. Strohmer, Compressed sensing radar, In: 2008 IEEE International Conference on Acoustics, Speech, and Signal Processing (ICASSP), Las Vegas, March 30–April 4, 2008, Nevada, USA, pp. 1509–1512.
11. M.A. Herman and T. Strohmer, High-resolution radar via compressed sensing, IEEE Trans Signal Process 57 (2009), 2275–2284.
12. I. Stojanovic, W.C. Karl, and M. Cetin, Compressed sensing of mono-static and multi-static SAR, In: Proc. Algorithms Synthetic Aperture Radar Imagery XVI, SPIE, 7337 (2009).
13. S. Bhattacharya, T. Blumensath, B. Mulgrew, and M. Davies, Fast encoding of synthetic aperture radar raw data using compressed sensing, In: The 2007 IEEE Workshop on Statistical Signal Processing, Madison, August 2007, pp. 448–452.
14. X.X. Zhu and R. Bamler, Tomographic SAR inversion by L1 –norm regularization: the compressive sensing approach, IEEE Trans Geosci Remote Sens 48 (2010), 3839–3846.
15. G. Rilling, M. Davies, and B. Mulgrew, Compressed sensing based compression of SAR raw data, In: Signal Processing with Adaptive Sparse Structured Representations—SPARS'09, Saint-Malo (F), 2009.
16. S.-J. Wei, X.-L. Zhang, J. Shi, and G. Xiang, Sparse reconstruction for SAR imaging based on compressed sensing, Prog Electromagn Res (PIER) 109 (2010), 63–81.
17. L. Yu and Y. Zhang, Random step frequency CSAR imaging based on compressive sensing, Prog Electromagn Res (PIER) C 32 (2012), 81–94.
18. Y. Lin, W. Hong, W.-X. Tan, et al., Compressed sensing technique for circular SAR imaging, In: IET International Radar Conference, Guilin, China, April 20–22, 2009.
19. C. Austin, E. Ertin, and R.L. Moses, Sparse multipass 3D imaging: Applications to the GOTCHA data set, In: Proc. SPIE 7337, Algorithms for Synthetic Aperture Radar Imagery XVI, 733703, April 28, 2009; doi:10.1117/12.820323.
20. C. Austin, E. Ertin and R.L. Moses, Sparse signal methods for 3-D radar imaging, IEEE J-STSP 5 (2011), 408–423.
21. Y.-S. Yoon and M.G. Amin, Compressed sensing technique for high-resolution radar imaging, In: Proc. SPIE 6968, Signal Processing, Sensor Fusion, and Target Recognition XVII, 69681A, April 17, 2008; doi:10.1117/12.777175.
22. H. Qiong, Q. Lele, W. Bingheng, F. Guangyou, UWB through-wall imaging based on compressive sensing, IEEE T Geosci Remote 48, (2010), 1408–1415.
23. M. Duman and A.C. Gurbuz, Performance analysis of compressive-sensing-based through-the-wall imaging with effect of unknown parameters, Int J Antenna Propag 2012 (2012), Article ID 405145, doi:10.1155/2012/405145.
24. E. Lagunas, M.G. Amin, F. Ahmad, M. Nájar, Compressive sensing for through wall radar imaging of stationary scenes using arbitrary data measurements, In: 11th International Conference on Information Science, Signal Processing and their Applications (ISSPA 2012), Montreal, QC, Canada, July 2–5, 2012, pp. 1347–1352.
25. A.C. Gurbuz, J. McClellan, and R. Scott, Jr., A compressive sensing data acquisition and imaging method for stepped frequency GPRs, IEEE Trans Signal Process 57 (2009), 2640–2650.
26. S.-J. Wei, X.L. Zhang, and J. Shi, Linear array SAR imaging via compressed sensing, Prog Electromagn Res (PIER) 117 (2011), 299–319.
27. V.M. Patel, G.R. Easley, D.M. Healy, Jr., and R. Chellappa, Compressed sensing for synthetic aperture radar imaging, In: IEEE International Conference on Image Processing (ICIP 2009), Cairo, Egypt, 2009, pp. 2141–2144.
28. C. Ozdemir, Inverse synthetic aperture radar imaging and its basic concepts, In: Inverse Synthetic Aperture Radar Imaging with MATLAB Algorithms, Chapter 7, John Wiley & Sons, Inc., Hoboken, NJ, 2012.
29. D. Needell and J.A. Tropp, CoSaMP: Iterative signal recovery from incomplete and inaccurate samples, Appl Comput Harmon A 26 (2009), 301–321.
30. S. Demirci, H. Cetinkay, E. Yigit, C. Ozdemir, and A. Vertiy, A study on millimeter-wave imaging of concealed objects: Application using back-projection algorithm, Prog Electromagn Res (PIER) 128 (2012), 457–477.

A COMPACT CPW-FED WIDE-SLOT ULTRAWIDEBAND ANTENNA WITH SHARP FREQUENCY REJECTION FUNCTIONS FOR WLAN BAND AND X-BAND

Yingsong Li,[1] Wenxing Li,[2] and Wenhua Yu[1,2]
[1] College of Information and Communications Engineering, Harbin Engineering University, Harbin 150001, China; Corresponding author: liyingsong@hrbeu.edu.cn
[2] 2COMU, Inc., State College, PA 16083

Received 26 April 2013

ABSTRACT: *In this article, a coplanar waveguide (CPW)-fed ultrawideband (UWB) antenna with two sharp frequency rejection functions is proposed. The dual band-notched characteristic is realized by etching a stepped impedance split-ring resonator (SISRR) and a stepped impedance resonator (SIR) in a circular radiating patch and a CPW transmission stripline, respectively. The central frequency of the two notch bands can be controlled by adjusting the SISRR and the SIR parameters. Simulation and experimental results obtained for this antenna show that it exhibits a good radiation behavior within the UWB frequency range and it also has the dual band-notched characteristics in the wireless local-area networks band and X-band, which can mitigate the potential interference between UWB systems and the designated existing narrow-band systems.* © 2013 Wiley Periodicals, Inc. Microwave Opt Technol Lett 55:2972–2976, 2013; View this article online at wileyonlinelibrary.com. DOI 10.1002/mop.27978

Key words: *UWB antenna; band-notched antenna; stepped impedance split-ring resonator; stepped impedance resonator*